Journal of Solid State Chemistry 182 (2009) 2319–2325

Contents lists available at ScienceDirect

Journal of Solid State Chemistry

journal homepage: www.elsevier.com/locate/jssc

New insight in the structure–luminescence relationships of $Ca_9Eu(PO_4)_7$

Rajia Ait Benhamou [a], Aurélie Bessière [a,*], Gilles Wallez [a], Bruno Viana [a], Mohamed Elaatmani [b], Mohamed Daoud [b], Abdelwahed Zegzouti [b]

[a] Laboratoire de Chimie de la Matière Condensée de Paris, CNRS-UMR7574, ENSCP-ParisTech, UPMC University, Paris 06, 11 rue Pierre et Marie Curie, 75231 Paris Cedex 05, France
[b] Laboratoire de la Matière Condensée et de l'Environnement, Université Cadi Ayyad, Faculté des Sciences-Semlalia, Marrakech, Morocco

ARTICLE INFO

Article history:
Received 26 January 2009
Received in revised form
9 June 2009
Accepted 10 June 2009
Available online 18 June 2009

Keywords:
Calcium phosphate
Crystal structure
Luminescence
Europium

ABSTRACT

The double phosphate $Ca_9Eu(PO_4)_7$, obtained by solid state reaction, was found to be isotypic with $Ca_3(PO_4)_2$, with space group *R*3*c* and unit cell parameters $a = 10.4546(1)$ Å, $c = 37.4050(3)$ Å, $V = 3540.67(9)$ Å^3, $Z = 6$. The structure parameters refined using the Rietveld method showed that europium shares positions *M*1, *M*2 and *M*3 with calcium, contradicting previously published Mössbauer results. Low temperature luminescence under selective excitation of Eu^{3+} in $Ca_9Y_{1-x}Eu_x(PO_4)_7$ and in $Ca_9Eu(PO_4)_7$ samples was studied, confirming the Eu^{3+} distribution into these sites. At 10 K, $^5D_0 \rightarrow {}^7F_0$ emission lines of Eu^{3+} were observed at 578.5, 579.5, 580.1 nm for the *M*3, *M*1 and *M*2 sites, respectively. High temperature X-ray powder diffraction evidenced a second-order phase transition around 573 °C.

1. Introduction

Tricalcium (bis) phosphate (TCP) β-$Ca_3(PO_4)_2$ is one of the most important biomaterials as it reproduces quite well the bone density. As such it is a good candidate for bioceramics [1,2]. In addition it is known to present an excellent thermal stability [3] and can be easily doped by trivalent ions as it offers various possibilities for doping by one-to four-fold cations [4]. Consequently, rare earth (*RE*) and transition metal (TM) ions-doped TCPs show high interest as optical materials. In powder form, these phosphates have been investigated for applications such as phosphors [5–7] or thermoluminescent dosimeters (TLD) for X-rays [8–13]. TCP is particularly suitable for TLD as it has an equivalent composition to human bones and teeth. Doped with Dy^{3+} or Tm^{3+}, the material absorbs X-rays in the way human tissues would do and stores charges before emitting light when thermally activated. Recently, we developed a new application in biological imaging for materials able to store charges and emit light after a delay: the use of red long-lasting phosphors as optical markers [14] was patented [15]. β-TCP:Eu^{3+} would be a good candidate for such an application. Finally as a crystal, β-TCP:Eu^{3+} might present an interest as a frequency-doubling material for non-linear applications.

However, despite the high interest in TCP for many optical applications, only very little is known on the dopant distribution. This knowledge is crucial as optical properties depend on dopant–dopant and/or dopant–defect interactions and a careful control of the dopant distribution in β-TCP would be required for the here above mentioned applications. The main purpose of the present work is to investigate the site occupancy of Eu^{3+} in heavily doped TCP, namely $Ca_9Eu(PO_4)_7$. $Ca_9Eu(PO_4)_7$ is isotypic of TCP, with a substitution scheme $(3Ca^{2+}) \rightarrow (2Eu^{3+} + 1\square)$ [16,17]. The structure of $Ca_3(PO_4)_2$ is rhombohedral with space group *R*3*c* ($a = 10.4352$ Å, $c = 37.4029$ Å) [18,19]. Five wide cationic positions exist, namely *M*1 to *M*5. Each of them is fully occupied with one Ca atom, except for the very small and irregular *M*4-oxygen polyhedron that has Ca deficiency. In $Ca_9Eu(PO_4)_7$, a precursor study by Mössbauer spectroscopy [20] indicated the occupation of two calcium sites by Eu^{3+}. Following, an optical analysis revealed the specific occupancy of *M*1, *M*2 and *M*3 sites [21]. In the present article, we analyze the site occupancy of Eu^{3+} in $Ca_9Eu(PO_4)_7$ by means of X-ray diffraction (XRD) and low temperature Eu^{3+} luminescence studies. Complementary structural data of thermal expansion are also given to conclude about crystal growth potentiality of the material.

2. Results and discussion

2.1. Experimental

$Ca_9Eu(PO_4)_7$ was synthesized by solid state reaction from a mixture of reagent-grade Eu_2O_3, $CaCO_3$ and $(NH_4)_2HPO_4$. After heating at 400 °C to remove H_2O, NH_3 and CO_2, the powder was ground in an agate mortar, pressed as a pellet and annealed in an alumina crucible at 1200 °C for 2×24 h with intermediate ball

* Corresponding author.
E-mail address: aurelie-bessiere@enscp.fr (A. Bessière).

0022-4596/$ - see front matter © 2009 Elsevier Inc. All rights reserved.
doi:10.1016/j.jssc.2009.06.018

milling, then cooled in the furnace. The room temperature diffraction pattern of $Ca_9Eu(PO_4)_7$ for structural analysis was recorded on a Panalytical X'Pert Pro diffractometer (main acquisition parameters are summarized in Table 1). High temperature diffraction for the dilatometric study was performed on a Philips PW1050/25 diffractometer with a Ni-filtered copper anticathode (40 kV, 20 mA), fitted with a Pt–Rh (40%) heating sample holder. Infrared spectra were recorded on a Bruker Tensor 27 spectrophotometer in the 400–4000 cm^{-1} range. For the optical analysis, the materials were stuck on a copper sample holder, which was mounted on the cold head of a closed cycle cryogenic refrigerator. The cold head was cooled to 10 K. Fluorescence and decay spectra were recorded using as excitation source an optical parametric oscillator laser (10 Hz, 8 ns) pumped by the third harmonic of a YAG:Nd laser. A Roper/Princeton ICCD detector was used to detect the fluorescence with a time delay set at 1 ms to eliminate the transition from the $^5D1$ to the $^7F_{0,1,2,3,4,5,6}$ state. Indeed at that time delay the $^5D_1$ transition which has a time constant in the order of the microsecond completely vanished.

Table 1
Data collection, refinement conditions and crystallographic data for $Ca_9Eu(PO_4)_7$.

Temperature (K)	298
Wavelength (Å), monochromator	$\lambda K\alpha$Cu = 1.540598, front Ge (111)
2θ range/step (deg)	9–140/0.013
Total counting time (h)	12
Number of data points	9976
Number of Bragg reflections	766
Number of *I*-dependent parameters	59
$R_P = \sum \lvert y_o^i - y_c^i \rvert / \sum y_o^i$	0.027
R_{WP} (id., weighted)	0.039
$R_{Bragg} = \sum \lvert I_o^i - I_c^i \rvert / \sum I_o^i$	0.052
$R_{exp} = ((n-p)/\sum w_i y_o^i)^{1/2}$	0.017
$R_F = \sum \lvert (I_o^i)^{1/2} - (I_c^i)^{1/2} \rvert / \sum (I_o^i)^{1/2}$	0.034
$\chi^2 = (R_{WP}/R_{exp})^2$	5.65
Space group	*R*3*c* (161)
a (Å)	10.4546(1)
c (Å)	37.4050(3)
V (Å^3)	3540.67(9)
Z	6
Density (calc.)	3.33

2.2. Structural study of $Ca_9Eu(PO_4)_7$

The X-ray diffraction pattern of the sample shows a single phase isotypic with β-$Ca_3(PO_4)_2$ (space group *R*3*c*). For steric reasons ($r_i(Eu^{3+}) = 1.07$ Å, $r_i(Ca^{2+}) = 1.12$ Å in eight-fold coordination [22]), trivalent europium is likely to share the same sites as divalent calcium, but the existence of five potential sites makes it difficult to estimate its distribution in the crystal structure, a crucial point regarding its optical properties. However, the strong electron density of the lanthanide, compared with calcium, should allow to measure its populations using Rietveld analysis.

All Rietveld analysis was carried out starting from the crystallographic data of the archetype [18]. The Fullprof program [23] was ran using the pseudo-Voigt profile function, but a slight broadening of the *l*-dependent peaks was observed and treated as a structural strain. This probably results from a disorder on the (Ca, Eu) sublattice, consistently with the absence of superstructure peaks. The final plot is shown in Fig. 1 with refinement parameters summarized in Table 1. The final atomic coordinates and Ca/Eu–O and Ca/Eu–Ca/Eu distances are reported in Tables 2 and 3.

Because the main goal of this study was to observe the Eu^{3+} distribution, a particular attention was paid to the reliability of the electron density measurements. The powder pattern of a non-doped β-$Ca_3(PO_4)_2$ sample was recorded and treated in the same conditions as for $Ca_9Eu(PO_4)_7$. We measured the occupancy rates for each five calcium sites separately, and found all of them to be within 3% of the ideal value. Considering the *Z* number of Eu (63 vs 20 for Ca), the error on its occupancy rate should be about 1%.

The crystal structure of $Ca_9Eu(PO_4)_7$ was first modelled as an all-calcium phosphate with variable occupancy rates for the five independent calcium atoms. This calculation evidences an excess of electron density due to the presence of heavier europium on sites *M*1, *M*2 and *M*3. On the contrary, *M*5 seems to be all-calcium, whereas *M*4, only half-occupied in TCP, appears empty in $Ca_9Eu(PO_4)_7$ (Table 2). This last observation means that, for stoichiometry reasons, all the other sites must be fully occupied. In the following refinement, we introduced europium on sites *M*1, *M*2 and *M*3 with complementary occupancy factors ($Ca_{1-x}Eu_x$), but without stoichiometric constraints on the global Eu/Ca ratio. Because of the reduced number of Bragg reflections, soft constraints were applied to the P–O bond lengths and O–P–O angles. We also gave the same thermal displacement factors to all

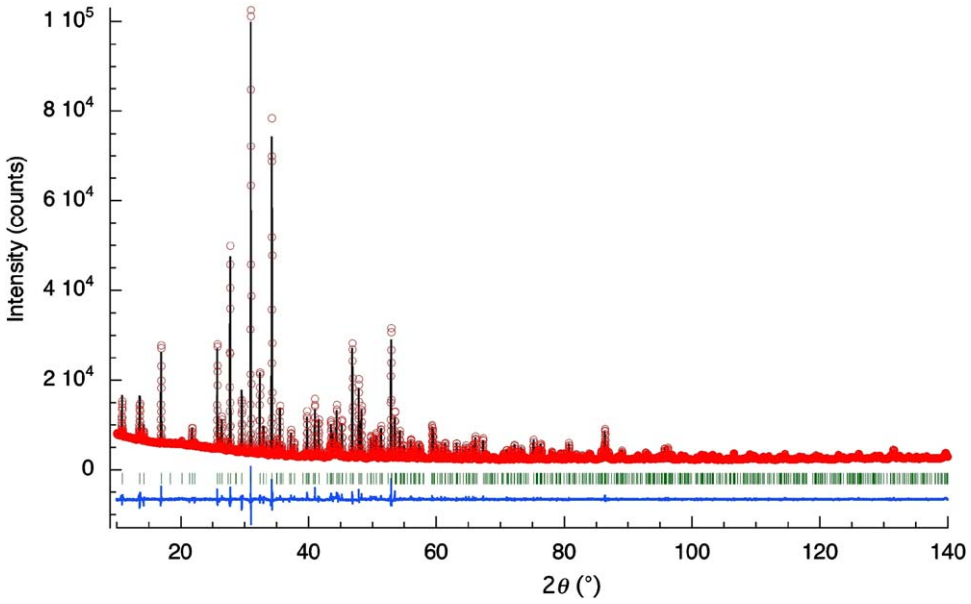

Fig. 1. Rietveld plot for $Ca_9Eu(PO_4)_7$: observed (circles), calculated (solid) and angular positions of possible Bragg reflections (bars). Lower plot: (I_c–I_o) difference curve.

Table 2
Positional and isotropic thermal parameters of $Ca_9Eu(PO_4)_7$.

Atom[a]	x	y	z	B_{iso} (Å^2)	Sites	Occupancy
Ca1	−0.2900(7)	−0.135(1)	0.1637(2)	0.14(2)	18*b*	0.841(5)
Eu1	−0.261(1)	−0.128(2)	0.1632(2)	0.14(2)	18*b*	0.159(5)
Ca2/Eu2	−0.3828(3)	−0.2019(5)	−0.0358(1)	0.14(2)	18*b*	0.893/0.107(5)
Ca3	−0.2729(4)	−0.1318(6)	0.0570(1)	0.14(2)	18*b*	0.932(2)
Eu3	−0.371(2)	−0.200(2)	0.0672(4)	0.14(2)	18*b*	0.068(2)
Ca5	0	0	−0.2685(2)	0.14(2)	6*a*	1[a]
P1	0	0	0	0.50(4)	6*a*	1
P2	−0.3183(3)	−0.1758(4)	0.1359(1)	0.50(4)	18*b*	1
P3	−0.3458(4)	−0.1894(4)	0.2368(1)	0.50(4)	18*b*	1
O1	−0.2768(5)	−0.1744(8)	−0.0958(1)	0.1(1)	18*b*	1
O2	−0.258(2)	−0.269(1)	−0.1531(3)	0.1(1)	18*b*	1
O3	−0.247(2)	−0.0141(7)	−0.1490(3)	0.1(1)	18*b*	1
O4	−0.4882(5)	−0.253(2)	−0.1437(3)	0.1(1)	18*b*	1
O5	−0.425(1)	−0.111(1)	−0.2197(3)	0.1(1)	18*b*	1
O6	−0.399(1)	−0.3436(9)	−0.2204(4)	0.1(1)	18*b*	1
O7	−0.1808(6)	−0.092(2)	−0.2248(3)	0.1(1)	18*b*	1
O8	−0.3589(7)	−0.190(1)	−0.2783(1)	0.1(1)	18*b*	1
O9	0.1351(7)	−0.0125(9)	−0.0114(3)	0.1(1)	18*b*	1
O10	0	0	0.0414(1)	0.1(1)	6*a*	1

[a] Calculated occupancy rates of sites *M*4 and *M*5 give, respectively, 0.00(1) and 0.97(1) Ca.

Table 3
Selected bond lengths and shortest Eu_i–Eu_j distances in $Ca_9Eu(PO_4)_7$.

Bonds	*d* (Å)		Bonds	*d* (Å)
Ca1–Eu1	0.28(1)		Ca3–Eu3	0.99(1)
Ca1/Eu1–O2	2.70(2)/2.68(2)		Ca3/Eu3–O1	[a]/2.82(2)
Ca1/Eu1–O3	2.73(2)/2.86(2)		Ca3/Eu3–O1	2.820(9)/ 2.40(2)
Ca1/Eu1–O4	2.52(1)/2.38(2)		Ca3/Eu3–O2	2.33(2)/ 2.48(2)
Ca1/Eu1–O4	2.47(2)/2.24(2)		Ca3/Eu3–O3	2.51(1)/ 2.29(2)
Ca1/Eu1–O5	2.34(1)/2.32(2)		Ca3/Eu3–O5	2.54(2)/ 2.67(2)
Ca1/Eu1–O6	2.39(2)/2.33(2)		Ca3/Eu3–O6	2.51(2)/ 2.25(2)
Ca1/Eu1–O8	2.26(1)/2.36(1)		Ca3/Eu3–O8	2.69(1)/ 2.92(2)
Ca1/Eu1–O9	2.33(1)/2.60(1)		Ca3/Eu3–O8	2.60(1)/[a]
			Ca3/Eu3–O9	2.88(1)/[a]
Ca2/Eu2–O1	2.455(7)		Ca3/Eu3–O10	2.539(4)/[a]
Ca2/Eu2–O2	2.32(1)			
Ca2/Eu2–O3	2.41(1)		Ca5–O4	2.25(1)
Ca2/Eu2–O5	2.78(2)		Ca5–O4	2.25(1)
Ca2/Eu2–O6	2.63(1)		Ca5–O4	2.25(1)
Ca2/Eu2–O7	2.45(1)		Ca5–O5	2.31(1)
Ca2/Eu2–O7	2.36(1)		Ca5–O5	2.31(1)
Ca2/Eu2–O9	2.377(9)		Ca5–O5	2.31(1)
Shortest cation–cation distances	Eu1	Eu2	Eu3	Ca5
Eu1	4.09 (× 2)	3.67 (× 1)	3.73 (× 1)	3.48 (× 1)
	6.37 (× 2)	3.88 (× 1)	4.29 (× 1)	6.41 (× 1)
		+4 at *d* < 7 Å	+7 at *d* < 7 Å	6.44 (× 1)
Eu2		4.46 (× 2)	3.86 (× 1)	3.57 (× 1)
		6.01 (× 2)	3.89 (× 1)	6.37 (× 1)
		+6 at *d* < 7 Å	+6 at *d* < 7 Å	6.55 (× 1)
Eu3			4.64 (× 2)	5.08 (× 1)
			5.85 (× 2)	5.39 (× 1)
			+6 at *d* < 7 Å	+2 at *d* < 7 Å
Ca5				All > 7 Å

[a] Distance > 3.3 Å; oxygen is not considered as bond to this cation.

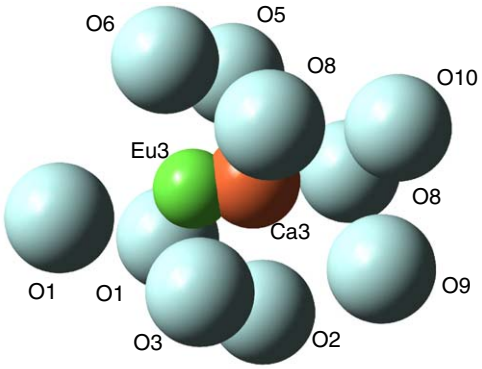

Fig. 2. The $M3O_{10}$ polyhedron, showing a strong splitting of the Ca/Eu positions. Note that left O1 is only bond to Eu; right O8, O9 and O10 are only bond to Ca.

atoms of the same species. At this point, the Fourier maps still evidence strong residual electron densities beside positions *M*1 and *M*3. After a new refinement with independent Ca/Eu atomic coordinates, the splitting of the position appears low for Ca/Eu2 (<0.06 Å, leading to consider a unique *M*2 site thereafter), moderate for Ca/Eu1 (0.28(1) Å) and strong for Ca/Eu3 (0.99(1) Å, Fig. 2).

The final reliability factors appear satisfactory, along with the sum of the occupancy factors, corresponding to 54.0(2)Ca and 6.0(2)Eu per cell, in agreement with the synthesis composition of 54Ca for 6Eu. Note that the given esd's are probably underestimated, because of the simplifications of the structural model.

Despite obvious similarities between $Ca_9Eu(PO_4)_7$ and β-$Ca_3(PO_4)_2$ (TCP), the substitution of calcium by europium and the emptiness of site *M*4 in the former induce secondary structural changes. Among the five sites occupied by calcium in the whitlockite structure, *M*4 singularizes by its very uncommon and inhospitable three-fold oxygen environment that results in an uncomplete sum of bond strengths: 0.65 v.u. using Brese's model [24]. On the opposite, the other sites offer more regular six- to nine-fold environments. Therefore, *M*4 is only half occupied (3/6) in TCP and, unsurprisingly, almost completely vacant in $Ca_9Eu(PO_4)_7$ insofar as $6Eu^{3+}$ and three vacancies have been substituted for $9Ca^{2+}$. It is noteworthy that in $Ca_9MH(PO_4)_7$ isotypes involving smaller bivalent cations (*M* = Mg [25,26], Mn [27]), the *M*4 site is also empty. Otherwise, Eu occupies sites *M*1, *M*2, *M*3, but not *M*5:

- 47% and 32% of the Eu atoms can be found, respectively, in the two eight-fold mean-sized sites *M*1 and *M*2, with moderate or low Ca/Eu splitting. Despite somewhat smaller, Eu behaves here like the host cation. The symmetry of sites *M*1 and *M*2 for Eu is C1.
- The roomy and elongated $M3O_{10}$ polyhedron allows a far stronger splitting with Eu3 occupying a low-coordination (7) off-centered position, consistently with its size. Only 20% occupy this site. The symmetry of *M*3 for Eu is also C1.
- The exclusive occupation of the small octahedral site *M*5 by the biggest atom (Ca) cannot be explained on the basis of steric arguments, but rather in terms of local equilibrium of charges. In the all-calcium structure, the bond valence sum of each oxygen ranges from 1.81 to 2.16 v.u., except for those forming the $M5O_6$ octahedron: 2.33 v.u. for O4 and 2.26 v.u. for O7. These outstandingly high values may be a strong repellent for trivalent cations like Eu^{3+}. On the contrary, in the pre-cited $Ca_9MH(PO_4)_7$ isotypes, the small divalent *M* cations ($r_i(Mg^{2+}) = 0.72$ Å, $r_i(Mn^{2+}) = 0.83$ Å in six-fold coordination, to be compared with $r_i(Eu^{3+}) = 0.95$ Å [22]) occupy exclusively the octahedral *M*5 site. Likewise, using single-crystal diffraction and EPR, Mayer et al. recently found Mn^{2+} exclusively in the *M*5 site of a manganese-doped TCP with formula $Ca_{2.85}Mn_{0.15}(PO_4)_2$ [28].

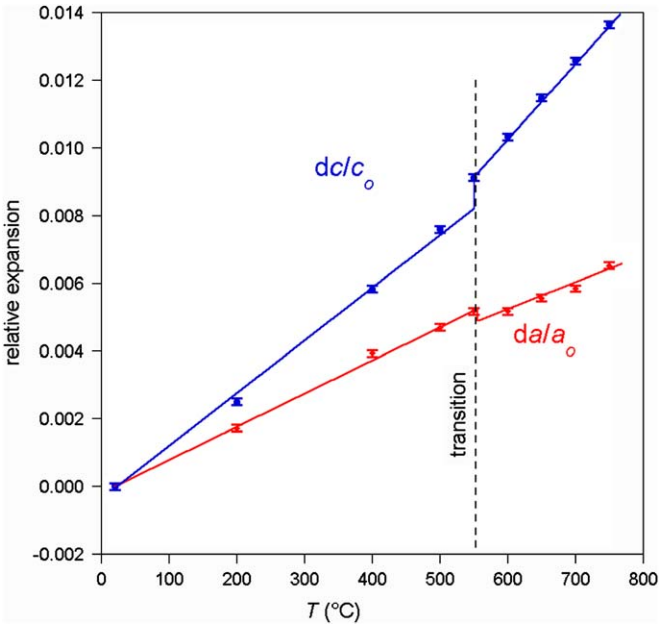

Fig. 3. Relative thermal expansion of the cell edges of $Ca_9Eu(PO_4)_7$ evidencing transition around 550 °C.

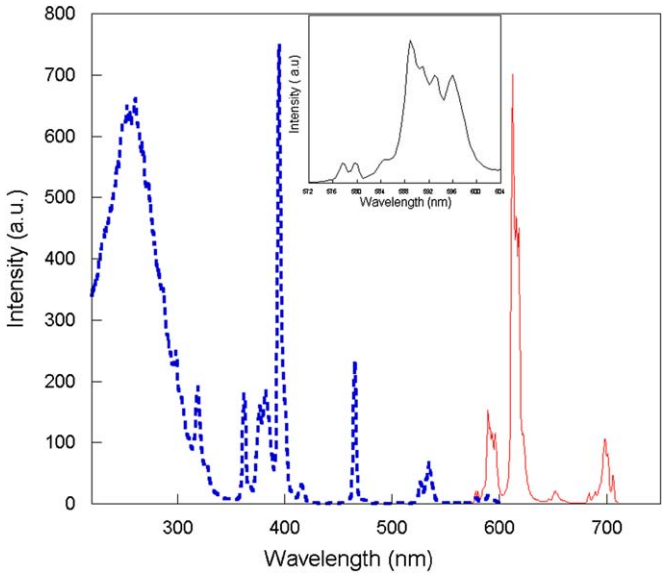

Fig. 4. Room temperature $Ca_9Eu(PO_4)_7$ emission spectrum (solid line) excited at 395 nm and excitation spectrum (dashed line) monitoring emission at 612 nm.

Finally, as shown in the lowest part of Table 3, the minimal possible Eu–Eu distance in $Ca_9Eu(PO_4)_7$ is 3.67 Å if two Eu ions occupy adjacent *M*1 and *M*2 sites. This minimal distance larger than those observed in pentaphosphate [29] is still sufficient to limit the *RE–RE* energy transfer. Then high light yield is expected in such compounds.

In the scope of a possible use as a single crystal material, $Ca_9Eu(PO_4)_7$ was studied by high temperature XRD analysis in the temperature range 20–750 °C. The cell parameters were refined by Rietveld analysis in Le Bail's (profile matching) mode and used to calculate coefficients of linear thermal expansion along the crystallographic axes *a* (α_a) and *c* (α_c).

The evolution of the cell parameters with temperature is shown in Fig. 3. A slight inflection is observed around 550 °C on both the $da/a_o = f(T)$ and the $dc/c_o = f(T)$ plots. Insofar as the powder pattern remains nearly unchanged, the inflection should correspond to the *R*3*c*–*R*–3*c* second order ferroelectric transition, already evidenced in other substituted TCPs [30–33]. Below 550 °C, the first temperature domain is characterized by the linear thermal expansion coefficients $\alpha_a = 9.1 \times 10^{-6}$ and $\alpha_c = 15.6 \times 10^{-6}\,K^{-1}$ and an average value $\alpha_l = (2\alpha_a + \alpha_c)/3 = 11.3 \times 10^{-6}\,K^{-1}$. Above 550 °C, the linear thermal expansion coefficients and average value are, respectively, 6.9×10^{-6}, 19.4×10^{-6} and $11.1 \times 10^{-6}\,K^{-1}$. A probable explanation for the strong expansion of the *c*-axis is given by the crystal structure made of short chains of face-connected CaO_n polyhedra extending parallel to this axis [18]. Such an array is commonly known to generate strong thermal longitudinal expansion because of the unscreened intercationic Coulombic interactions. On the contrary, in the (001) plane, the polyhedra are only connected by edges, thus giving moderate expansion.

Concerning the growth of single crystals from the melt for further applications, the observed second order phase transition seems moderate enough to avoid risks of breaking. The major concern is the strong α_c coefficient, which requires a slow cooling both before and after the phase transition.

2.3. Optical properties of $Ca_9Eu(PO_4)_7$

Room temperature $Ca_9Eu(PO_4)_7$ emission and excitation spectra in the visible range are presented in Fig. 4. The excitation spectrum exhibits a broad absorption band peaking at 257 nm attributed to $O(2p) \rightarrow Eu^{3+}$ charge transfer which is the main band for the UV excitation when used as a phosphor. Narrow absorption and emission bands located above 350 nm are characteristic of Eu^{3+} 4*f*–4*f* parity forbidden transitions. The inset of Fig. 4 zooms on the 575–610 nm emission range. It shows around 580 nm a low intensity massif corresponding to $^5D_0 \rightarrow {}^7F_0$ transitions and around 590 nm a higher intensity massif corresponding to $^5D_0 \rightarrow {}^7F_1$ transitions. One can distinguish two unresolved bands in the $^5D_0 \rightarrow {}^7F_0$ spectral range.

To go deeper into the analysis, the low temperature optical spectroscopy of 2%, 6% and 100% Eu^{3+} in $Ca_9Y_{1-x}Eu_x(PO_4)_7$ powdered samples was performed. This corresponds to europium concentrations of, respectively, 3.4×10^{19}, 1×10^{20} and 1.7×10^{21} at/cm^3. Laser excitation was performed at 10 K at 525 nm in the $^7F_0 \rightarrow {}^5D_1$ transition or at about 580 nm in the $^7F_0 \rightarrow {}^5D_0$ transition. Fig. 5 presents the emission spectra under selective excitation for 2%Eu:$Ca_9Y(PO_4)_7$. Three contributions at 578.5, 579.7 and 580.2 nm are clearly observed for the $^5D_0 \rightarrow {}^7F_0$ transition, corresponding to three different sites occupancy. Similar results are obtained for 6%Eu:$Ca_9Y(PO_4)_7$ and for $Ca_9Eu(PO_4)_7$ as presented in Fig. 6. The occupancy of the same site is not surprising as the cations size for Y^{3+} and Eu^{3+} are very close. In order to compare structural data presented at the beginning of the paper and optical properties with the best signal over noise ratio possible, we focused our analysis on the $Ca_9Eu(PO_4)_7$ compound in the following part of the paper.

Emission spectra of $Ca_9Eu(PO_4)_7$ were recorded at 10 K under laser excitation at 525 and around 580 nm, i.e. in the $^7F_0 \rightarrow {}^5D_1$ and $^7F_0 \rightarrow {}^5D_0$ transitions, respectively. They are shown in Fig. 6 and the different emission massifs are assigned to the $^5D_0 \rightarrow {}^7F_{0,1,2}$ transitions of Eu^{3+}. When excited at 525 nm in the $^7F_0 \rightarrow {}^5D_1$ transition (see Fig. 6(a)), the emission spectrum is composed of the superposition of several site contributions while under selective excitation at 578.5, 579.5 or 580.1 nm (see, respectively, Fig. 6(b), (c) and (d)) it is possible to analyze the contribution of three sites separately. The inset of Fig. 6 zooming on spectrum (a) around 580 nm shows that the $^5D_0 \rightarrow {}^7F_0$ emission massif presents three characteristic lines at 578.5, 579.5 and 580.1 nm similar to the emission bands presented in Fig. 5. These three lines were attributed to three crystallographic sites labelled *A*, *B* and *C*, respectively. The (b), (c) and (d) emission spectra recorded under

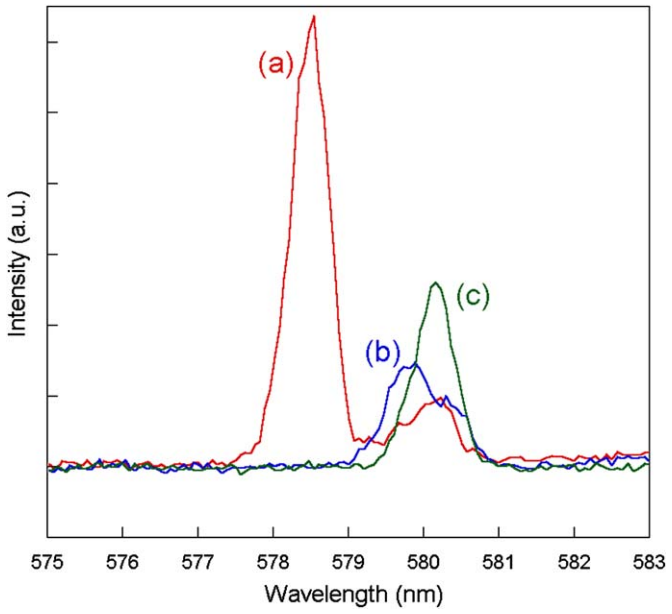

Fig. 5. 10 K emission spectra of 2%: $Ca_9Y(PO_4)_7$ under excitation in the $^5D_0 \rightarrow {}^7F_0$ transition: at 578 (a), 579 (b) and 580 nm (c). The emission is recorded 1 ms after the laser excitation.

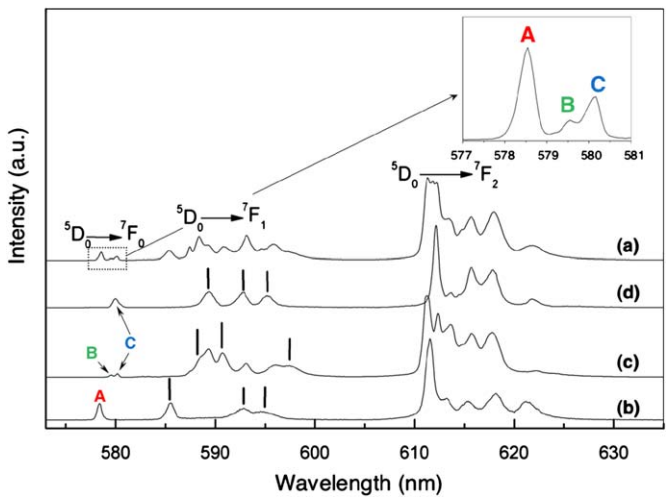

Fig. 6. Emission spectra of $Ca_9Eu(PO_4)_7$ recorded at 10 K, excited at (a) 525 (*A*, *B* and *C* sites), (b) 578.5 (*A* site), (c) 579.5 (*B* and *C* sites) and (d) 580.1 nm (*C* site). A 1 ms delay between laser excitation pulse and luminescence measurement was used to prevent observation of the $^5D_1$ emission at shorter wavelengths.

Table 4
Energy level positions of Eu^{3+} in $Ca_9Eu(PO_4)_7$ identified from the 10 K emission spectra of Fig. 6.

Site	$^5D_0 \rightarrow {}^7F_0$	$^5D_0 \rightarrow {}^7F_1$	$^5D_0 \rightarrow {}^7F_2$
A (nm)	578.5	585.4, 592.8, 594.7	611.5, 613.3, 615.3, 618.1, 621.2
B (nm)	579.5	587.4, 591, 597.3	611.1, 613.3, 614.9, 618.1, 624.3
C (nm)	580.1	588.4, 593.5, 595.8	612.1, 613.6, 615.6, 617.8, 621.8

excitation in the three sites led to the attribution of the energy levels underlined with bars in Fig. 6 and reported in Table 4. The $^5D_0 \rightarrow {}^7F_1$ emission massif excited at 525 nm (spectrum (a)) is actually composed of nine lines corresponding to the superposition of the three lines for each of the *A*, *B* and *C* sites. According to Antic et al. [34], a correlation between the

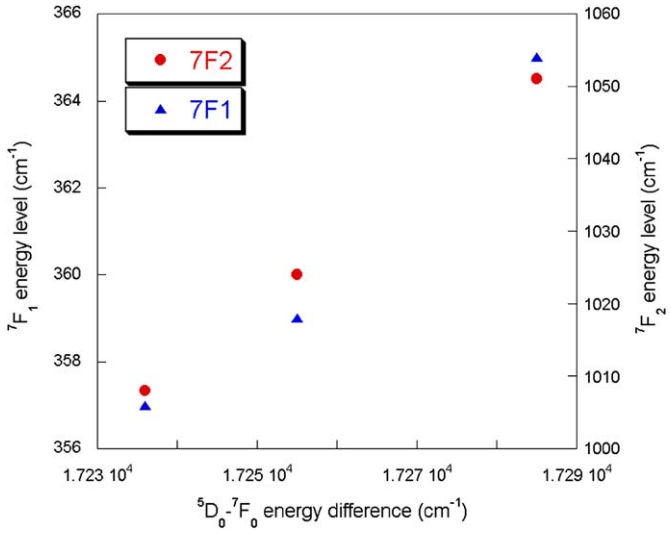

Fig. 7. Barycenters energy of the $^7F_1$ and $^7F_2$ levels of Eu^{3+} in $Ca_9Eu(PO_4)_7$ as a function of the energy of the $^7D_0$–$^7F_0$ transition, illustrating the "barycenter law". The $^7F_0$ level is taken as the energy reference and indicated in cm^{-1}. The three points represent sites *A*, *B* and *C*.

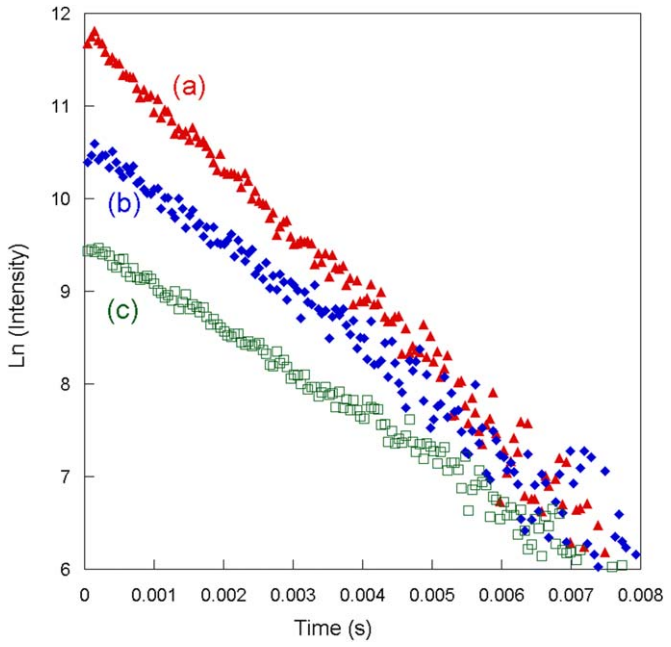

Fig. 8. 10 K emission decay profiles of $Ca_9Eu(PO_4)_7$ recorded at 578.5 (a), 580 (b) and 580.5 nm (c).

barycenters of the various energy levels is expected due to the spin orbital interaction, while the energy level splitting is related to the crystal field interaction and is host dependent. The barycenters of the energy levels for the *A*, *B* and *C* sites are presented in Fig. 7. A very good correlation for the $^7F_0$, $^7F_1$ and $^7F_2$ levels could be drawn, confirming the position of the energy levels reported in Table 4.

Luminescence decay measurements of the $^5D_0 \rightarrow {}^7F_0$ emission from the *A*, *B* and *C* sites performed at 10 K are presented in Fig. 8. They all show an exponential behavior. A short decay value of 1.4 ms was observed for the emission at 578.5 nm (*A* site) while longer lifetimes around 1.8 ms were found at 580.0 and 580.5 nm (*B* and *C* sites). In the following, we will attempt to correlate the *A*, *B* and *C* sites observed in spectroscopy with the actual *M* sites of the material available for Eu^{3+} according to the

structural study, i.e. *M*1, *M*2 and *M*3. The following arguments were used:

(i) According to the literature and the so-called nephelauxetic effect [34], the position in energy of the $^7F_0 \rightarrow {}^5D_0$ lines for non-equivalent Eu^{3+} centers is related to the mean length of the Eu–O bond. When Eu–O distances increase, the $^7F_0 \rightarrow {}^5D_0$ transition shifts toward shorter wavelengths (higher energy). On the opposite, a red shift is observed with an increase of covalency.
(ii) The splitting of the $^7F_1$ or $^7F_2$ levels is characteristic of the crystal field strength [35]. As the Eu–O mean distance decreases, the crystal field as well as the splitting of the $^7F_1$ and $^7F_2$ energy levels increase.
(iii) For a given emitting ion, long decay time is characteristic of the most symmetrical surrounding while short decay values are observed when site distortion occurs.
(iv) Site symmetry also influences the $^5D_0 \rightarrow {}^7F_2/{}^5D_0 \rightarrow {}^7F_1$ intensity ratio which corresponds to an "asymmetry" parameter. The $^5D_0 \rightarrow {}^7F_2/{}^5D_0 \rightarrow {}^7F_1$ intensity ratio increases when the contribution of the electrical dipolar interaction in the transition probability increases. This effect is related to distortion occurring in the europium surrounding [29].
(v) Increased intensity of the forbidden $^5D_0 \rightarrow {}^7F_0$ transition relative to the $^5D_0 \rightarrow {}^7F_1$ intensity reveals distortion [29].

Data relative to these arguments for *A*, *B* and *C* sites are reported in the first half of Table 5. The second half presents data relative to *M*2, *M*1 and *M*3 sites.

Site *A* presents the most blue-shifted $^5D_0 \rightarrow {}^7F_0$ transition (argument (i)), medium $^7F_1$ crystal field splitting and the lowest $^7F_2$ crystal field splitting (argument (ii)) therefore implying a quite low covalency site. In addition site *A* presents the shortest lifetime (1.40 ms) (argument (iii)), the largest $^5D_0 \rightarrow {}^7F_2/{}^5D_0 \rightarrow {}^7F_1$ emission ratio (3.3) (argument (iv)) and the most intense $^5D_0 \rightarrow {}^7F_0$ emission (argument (v)). Then the most likely assignment for site *A* is a quite low covalency and above all a quite distorted site, i.e. *M*3. *M*3 shows the longest mean Eu–O distance and its surrounding is 7+3 oxygen with large distance variation around the mean Eu–O distance. In Table 3, one Eu–O distance is significantly longer (2.92 Å) than all the others and two are significantly shorter (2.25 and 2.29 Å).

The assignment of *B* and *C* positions is less straightforward between *M*1 and *M*2 as lifetime values are similar. However from Table 3, even if the mean Eu–O distances are the same for these two sites, *M*2 presents the most symmetrical europium site and one can assume that the covalency should therefore be stronger in *M*2 than in *M*1. A redshift for the $^5D_0 \rightarrow {}^7F_0$ transition is expected according to the nephelauxetic effect [34]. *M*2 may therefore correspond to site *C*, presenting a small value of the $^5D_0 \rightarrow {}^7F_2/{}^5D_0 \rightarrow {}^7F_1$ emission ratio (relative to site *A*), the most redshifted $^5D_0 \rightarrow {}^7F_0$ transition and a small splitting of the $^7F_1$ level (relative to site *A*). *B* position is therefore attributed to *M*1 with a slightly larger value of the $^7F_1$ energy level splitting (281 cm^{-1}). This is probably linked to the larger variation of the Eu–O distances and there is in particular a short Eu–O distance of 2.24 Å for *M*1.

In conclusion, we are able to propose a location for the trivalent europium cations in $Ca_9Eu(PO_4)_7$ within three different sites taking into account both structural analysis and optical spectroscopy results. The three sites are *M*3 (band A in Fig. 6), *M*1 (band B), and *M*2 (band C). *M*5 is not occupied with Eu^{3+}.

Table 5
Data from optical spectroscopy and from structural characterization of the three crystallographic sites observed for Eu^{3+} in $Ca_9Eu(PO_4)_7$.

Optical spectroscopy	*A*	*B*	*C*
Energy levels $^5D_0 \rightarrow {}^7F_0$ transition (cm^{-1})	17 285	17 255	17 236
$^7F_1$ barycenter (cm^{-1})	365	359	357
$^7F_1$ energy level splitting (cm^{-1})	266	281	214
$^7F_2$ barycenter (cm^{-1})	1051	1024	1008
$^7F_2$ energy level splitting (cm^{-1})	295	310	254
Lifetime (ms) of $^5D_0 \rightarrow {}^7F_0$	1.40	1.85	1.80
$^5D_0 \rightarrow {}^7F_2/{}^5D_0 \rightarrow {}^7F_1$ ratio	3.3	2.8	2.8
Intensity of $^5D_0 \rightarrow {}^7F_0$	+++	+	++
Structural characterization	*M*3	*M*1	*M*2
Site occupancy	+	+++	++
Mean Eu–O distance (Å)	2.54(7)	2.47(1)	2.47(3)
(number of neighbours)	(7+3)	(8)	(8)
Site distortion	++	+	+

3. Conclusion

$Ca_9Eu(PO_4)_7$ is isotypic with β-$Ca_3(PO_4)_2$, with Eu^{3+} substituted for Ca^{2+}. At variance with previous Mössbauer studies [20] which attributed only two different sites to Eu^{3+}, our Rietveld analysis allowed to localize the dopant in *M*1, *M*2 and *M*3 sites instead in agreement with [21]. *M*5 site appears exclusively occupied by Ca and unstable *M*4 site is empty. This distribution, in good agreement with sterical criteria and charge balance considerations, is supported by optical measurements. The low temperature Eu^{3+} emission bands were attributed to the three types of calcium sites occupied by Eu^{3+}. The attribution are the following, *M*3 for band A, *M*1 for band B, and *M*2 for band C (see Fig. 6).

Such a distribution implies long distances between *RE* even at high concentration and therefore weak concentration quenching of Eu^{3+} luminescence making $Ca_9Eu(PO_4)_7$ an efficient phosphor. For a more specific application like thermoluminescence dosimetry or long-lasting phosphorescence α-$Ca_3(PO_4)_2$ could be doped by Eu^{3+} as the luminescence center and co-doped by a trapping center. In that case, the knowledge of the site distribution over the different sites of the structure will be useful to deeply analyze the luminescence mechanisms.

Finally we have also demonstrated that the elaboration of single crystals may be considered, insofar as the ferroelectric transition around 550 °C is clearly second-order which is the more favorable case, but care should be taken on cooling because of the strong expansion along the *c*-axis.

Acknowledgments

These research works have been developed under a bilateral research program Volubilis between the LCSM University Cadi Ayyad, Marrakech-Morocco and the LCPMC-UPMC Paris-France.

References

[1] S.V. Dorozhkin, M. Epple, Angew. Chem. Int. Ed. 41 (2002) 3130.
[2] L.L. Hench, J. Am. Ceram. Soc. 74 (2005) 1487.
[3] W. Pan, G. Ning, X. Zhang, J. Wang, Y. Lin, J. Ye, J. Lumin. 128 (2008) 1975.
[4] B. Lazoryak, V.A. Morozov, A.A. Belik, J. Solid State Chem. 122 (1996) 15.
[5] K. Maeda, J. Phys. Soc. Jpn. 14 (1959) 478–486.
[6] H.C. Froelich, J.M. Margolis, J. Electrochem. Soc. 98 (1951) 400.
[7] E.J. Kim, S.W. Choi, S.H. Hong, J. Am. Ceram. Soc. 90 (2007) 2795.
[8] H. Ohtaki, Y. Fukuda, N. Takeuchi, Radiat. Prot. Dosim. 47 (1993) 119.
[9] K. Mizuguchi, Y. Fukuda, Radiat. Prot. Dosim. 84 (1999) 301.
[10] Y. Fukuda, H. Ohtaki, S. Taniguchi, N. Takeuchi, J. Mater. Sci. Lett. 11 (1992) 731.
[11] Y. Fukuda, Radiat. Prot. Dosim. 33 (1990) 151.
[12] Y. Fukuda, H. Ohtaki, S. Owaki, Phys. Stat. Sol. 144 (1994) 107.
[13] K. Madhukumar, H.K. Varma, M. Komath, T.S. Elias, V. Padmanabhan, C.M.K. Nair, Bull. Mater. Sci. 30 (2007) 527.

[14] Q. Le Masne, D. Scherman, M. Bessodes, F. Pellé, S. Maitrejean, J.-P. Jolivet, C. Chanéac, D. Gourier, Proc. Nat. Acad. Sci. USA 104 (2007) 9266.
[15] Q. Le Masne, D. Scherman, M. Bessodes, F. Pellé, S. Maitrejean, J.-P. Jolivet, C. Chanéac, D. Gourier, Nanoparticules à luminescence persistante pour leur utilisation en tant qu'agent de diagnostique destiné à l'imagerie optique in vivo. Patent, WOEP06067950, WO2007048856, 30/10/2006.
[16] V.N. Golubev, B.I. Lazoryak, Inorg. Mater. 27 (1991) 480.
[17] B.I. Lazoryak, Russ. Chem. Rev. 65 (1996) 287.
[18] M. Yashima, A. Sakai, T. Kamiyama, A. Hoshikawa, J. Solid State Chem. 175 (2003) 272.
[19] B. Dickens, L.W. Shroeder, W.E. Brown, J. Solid State Chem. 10 (1974) 232.
[20] B.I. Lazoryak, B.N. Witing, P.B. Fabrichnyi, L. Furnes, R. Salmon, P. Hagenmuller, Kristallografiya 35 (1990) 1403.
[21] B.I. Lazoryak, V.N. Golubev, Eur. J. Solid State Inorg. Chem. 26 (1989) 455.
[22] R.D. Shannon, Acta Crystallogr. A 32 (1976) 751.
[23] J. Rodriguez-Carvajal, FULLPROF.2k, Rietveld, Profile Matching and Integrated Intensity Refinement of X-ray and Neutron Data, Laboratoire Léon Brillouin, CEA, Saclay, France, 2001.
[24] N.E. Brese, M. O'Keeffe, Acta Crystallogr. B 47 (1991) 192.
[25] B. Dickens, L.W. Shroeder, W.E. Brown, J. Solid State Chem. 10 (1974) 232.
[26] R. Gopal, C. Calvo, J. Ito, W.K. Sabine, Can. J. Chem. 52 (1974) 1155.
[27] E. Kostiner, J.R. Rea, Acta Crystallogr. B 32 (1976) 250.
[28] I. Mayer, S. Cohen, S. Gdalya, O. Burghaus, D. Reinen, Mater. Res. Bull. 43 (2008) 447.
[29] F. Auzel, J. Dexpert-Ghys, C. Gautier, J. Lumin. 27 (1) (1982) 1–12.
[30] G. Blasse, B.C. Grabmaier, Luminescent Materials, Springer, Berlin, 1994.
[31] B.I. Lazoryak, V.A. Morozov, A.A. Belik, S.Y. Stefanovich, V.V. Grebenev, I.A. Leonidov, E.B. Mitberge, S.A. Davydov, O.I. Lebedev, G. van Tendeloo, Solid State Sci. 6 (2004) 185.
[32] V.A. Morozov, A.A. Belik, S.Y. Stefanovich, V.V. Grebenev, O.I. Lebedev, G. van Tendeloo, B.I. Lazoryak, J. Solid State Chem. 165 (2002) 278.
[33] A.A. Belik, F. Izumi, S.Yu. Stefanovich, A.P. Malakho, B.I. Lazoryak, I.A. Leonidov, O.N. Leonidova, S.A. Davydov, Chem. Mater. 14 (2002) 3197.
[34] E. Antic-Fidancev, J. Alloys Compds. 300 (2000) 2.
[35] F. Auzel, O. Malta, J. Phys. 44 (1983) 201.